Applied Catalysis A: General 483 (2014) 85–96

Contents lists available at ScienceDirect

Applied Catalysis A: General

journal homepage: www.elsevier.com/locate/apcata

Screening iridium-based bimetallic alloys as catalysts for direct ethanol fuel cells

Julien Courtois[a], Wenxin Du[b], Emily Wong[b], Xiaowei Teng[b], N. Aaron Deskins[a,*]

[a] Department of Chemical Engineering, Worcester Polytechnic Institute, 100 Institute Road, Worcester, MA 01609, United States
[b] Department of Chemical Engineering, University of New Hampshire, Durham, NH 03824, United States

ARTICLE INFO

Article history:
Received 13 May 2014
Received in revised form 23 June 2014
Accepted 29 June 2014
Available online 7 July 2014

Keywords:
Iridium
Alloys
Fuel cell
Ethanol oxidation
Density functional theory

ABSTRACT

Current ethanol oxidation catalysts in direct ethanol fuel cells (typically platinum-based) suffer from low conversion and are susceptible to CO poisoning. We therefore determined to find viable alternative catalysts for ethanol oxidation based on iridium using density functional theory to model bimetallic alloy (1 1 1) surfaces. Iridium was alloyed with another transition metal (from groups 4 through 11), M, in an overlayer (one layer of metal M on top of bulk iridium) or subsurface configuration (M inserted under the first layer of iridium). Segregation energies were calculated and the subsurface configuration was found to be most stable configuration in the majority of alloy cases under vacuum conditions. Select alloys (including Ir–Pt and Ir–Rh) showed a reversal of preferred alloy state (overlayer or underlayer) upon adsorption of CO. CO adsorption was modeled and lower CO adsorption energies were found for many alloys compared to pure Pt, indicating less CO poisoning. Complete oxidation of ethanol is typically limited by the breaking of strong C—C bonds, so any catalyst must lower the barriers for C—C bond breaking. Activation energies for C—C bond breaking (by considering a representative intermediate molecule CHCO) were lowered for the vast majority of the alloys used in an underlayer structure, reinforcing the significance of the underlayer structures or "subsurface" alloys. Finally, we found, based on CO adsorption energy, activation energy for C—C breakage reaction, and metal cost, three important catalyst descriptors, a number of promising catalysts for the ethanol oxidation reaction, such as alloys with M = Zr, Nb, Mo, W, Ru, Os, or Re. Experimental verification (cyclic voltammetry and chronoamperometry for ethanol oxidation) on Ir, Ir–Ru, and Ir–Rh catalysts confirmed the superiority of these Ir-based catalysts compared to Pt. Our results demonstrate that alloys of Ir show promise as more affordable substitutes for platinum group metals.

1. Introduction

The world's energy demand is continually growing, and it is crucial to find alternatives to current fossil fuels. Indeed, more efficient and environmental friendly energy production processes are needed. Numerous solutions are currently being investigated including fuel cells, which may produce energy with low environmental footprint. Polymer electrolyte membrane (PEM) fuel cells have large theoretical efficiency when a fuel, such as hydrogen is supplied to the device, much more than combustion, which is limited by the Carnot cycle efficiency [1]. Nevertheless, the problem of storage currently hinders the use of hydrogen as a fuel. For example, storage may require high pressure tanks operating at 200–700 bar, or a cryogenic tanks working at low temperatures (such as −223 °C) [2,3]. Chemical storage of hydrogen has also being investigated, but is difficult. Other fuels have been considered, including alcohols such as ethanol or methanol. Ethanol is an attractive fuel choice because it is easily stored as a liquid and has high energy density [1,4–6], similar to gasoline's energy density [7]. Ethanol is also relatively non-toxic. Furthermore, ethanol can be produced in important quantities from biomass [5].

Slow kinetics for the ethanol oxidation reaction (EOR) at the anode catalyst limits the efficiency of direct-ethanol fuel cells (DEFCs). For example, over current Pt-based catalysts incomplete oxidation of ethanol produces acetaldehyde and acetic acid which releases only 2 and 4 electrons, respectively [1,4]. Complete oxidation however forms CO_2 and releases 12 electrons [1,4], increasing the available electrical energy, as indicated by the following reactions:

$$CH_3CH_2OH + 3H_2O \rightarrow 12H^+ + 12e^- + 2CO_2 (\text{totaloxidation}) \quad (1)$$

* Corresponding author. Tel.: +1 508 8315445.
E-mail address: nadeskins@wpi.edu (N.A. Deskins).

http://dx.doi.org/10.1016/j.apcata.2014.06.029
0926-860X/

$$2CH_3CH_2OH + H_2O \rightarrow 6H^+ + 6e^- + CH_3COOH + CH_3CHO(\text{partialoxidation}) \quad (2)$$

Current Pt-based catalysts are expensive and also suffer from CO poisoning. It is therefore necessary to find new electrocatalysts that could increase the overall kinetics of the ethanol oxidation reaction and increase the selectivity of the reaction toward CO_2 formation [3]. DEFC anode catalysts have been extensively studied, with much focus on platinum. Various attempts have been employed to reduce the Pt loading, such using alloys or carbon supports or even using other materials like carbides and oxides as anode catalysts. Alloying, by adding another element [3,5,8–10] or by even adding a third element [5], has been a popular method of catalyst development. Different alloy structures have been studied, from metal doping to near surface alloys (NSA) [11] or even core/shell structures [12,13].

The bottleneck for efficient ethanol oxidation is believed to be the breaking of strong C—C bonds [3]. Various C—H, C—O, or C—C scission steps may occur at the catalyst surface, but complete oxidation involves C—C bond breaking, while incomplete oxidation does not. Density functional theory (DFT) calculations are commonly used to identify new potential catalysts and numerous studies have been performed for ethanol oxidation/decomposition [14–17]. Ferrin et al. [18] screened various transitions metals as catalysts for ethanol decomposition using Brønsted–Evans–Polanyi (BEP) correlations to determine the activation barriers for possible intermediates and they have been able to show that, for most transitions metals, including iridium, the rate determining step for C—C cleavage involves a CHCO intermediate being separated into two molecules, CH and CO. Another previous DFT study led by Alcala et al. [15] investigated C—O and C—C cleavage pathways over Pt for ethanol and concluded that C—C scission was also likely to proceed through a ketenyl species (CHCO).

Platinum group metals are well known for their exceptional catalytic properties. Ferrin et al. [18] reported that metals such as Pt, Pd, Ru, Ir or Rh could be interesting candidates for the EOR. Many experimental or theoretical studies can be found in the literature concerning Pt [10,19–21], Pd [6], Ru [22–24] and Rh [3] as catalysts for the EOR but less work has been conducted with Ir. Recent experimental work with Ir and Sn was reported [25] and showed comparable results to that of a Pt_3Sn/C catalyst, currently one of the most efficient anode catalysts for the EOR [10,16]. More recently, Du et al. [4] also showed that Ir (in the form of Ir–Sn–SnO_2) could be a very good catalyst candidate for the EOR, obtaining a high electrochemical activity comparable to a commercial PtSn catalyst. They observed a core–shell structure for the Ir alloy. The same group developed a Ir–Ru alloy [26] which showed enhanced activity compared to Pt or Ir.

Motivated by previous experimental and theoretical work, the reactivity of Ir-based catalysts for the EOR has been investigated, using core–shell-like bimetallic structures made of Ir and another transition metal. Emphasis was placed on C—C bond breaking as a potential rate determining step ($CHCO \rightarrow CH + CO$) and in identifying potential catalysts to replace Pt. Our efforts focused on modeling a large number of alloys and screening these alloys for potential ethanol oxidation activity. Accordingly, activation energies were calculated using a previously established BEP correlation [27]. We also examined the resistance of the studied alloys to CO adsorption. The preferred location of alloyed metals (surface or sub-surface) was examined and we determined under what conditions such alloys are stable. Our analysis indicates which alloys would potentially be economically feasible and also catalytically active, suggesting directions for future experimental studies.

2. Methodology

2.1. Computational methodology

2.1.1. Simulation parameters

All calculations were performed using the CP2K code [28,29]. The PBE exchange correlation function was used [30]. CP2K uses the Gaussian and Plane Wave (GPW) [31] method so electron densities were treated by plane wave functions and molecular orbital were represented by double-zeta Gaussian basis functions [32]. Core electrons were represented by Goedecker–Teter–Hutter (GTH) pseudopotentials [33,34]. The current version of CP2K only samples reciprocal space at the Γ point, which could potentially result in simulations errors. Consequently, the slab that we used was rather large so any errors from k-point sampling were minimized. With the exception of Ni, Co, and Fe, which display magnetic properties, all bimetallic structures were modeled as non-spin polarized, similar to previous work [35]. For instance, we calculated the CO adsorption energy over a Au–Ir alloy to differ by only 10^{-4} eV between spin polarized and non-spin polarized calculations.

2.1.2. Surface model

The Ir (1 1 1) surface was modeled using the slab approach, with a 6×6 super cell under periodic boundary conditions. Each slab was repeated periodically with at least 30 Å of vacuum between neighboring metal slabs and was three atomic layers thick. The bottom layer of the slab was kept frozen. Two different alloys configurations were used as shown in Fig. 1: the first configuration consisted of replacing the top layer of Ir with another transition metal (overlayer structure), while the second consisted of replacing the middle Ir layer with another transition metal (underlayer structure). Similar alloy structures were used by Greeley and Mavrikakis [11] or by Su et al. [8] in their study of near-surface alloys. Adsorption was allowed only on the top layer of the slab. Transition metals between groups 4 (Ti, Zr, and Hf) and 11 (Cu, Ag, and Au) of the periodic table were all alloyed with Ir.

Adsorption energies were determined according the following formula:

$$E_{\text{adsorption}} = E_{\text{adsorbate/surface}} - E_{\text{surface}} - E_{\text{adsorbate in gas phase}} \quad (3)$$

where $E_{\text{adsorbate/surface}}$ is the energy of the surface/adsorbate system, E_{surface} is the energy of the clean surface, and $E_{\text{adsorbate in gas phase}}$ is the energy of the gas-phase molecule. We modeled adsorption of CO, CH, and CHCO over the various alloys. As previously mentioned, C—C bond breaking is typically the hardest step in the ethanol oxidation reaction. Work by Alcala et al. [15] showed that C—C breaking of CHCO had the lowest barrier of various possible intermediates over the Pt (1 1 1) surface. Later work by Ferrin et al. [18] expanded to other (1 1 1) surfaces, including Ir. The rate-determining step was found to also involve CHCO C—C scission. Hence, we modeled CHCO adsorption and its derivatives. CO was adsorbed on top sites, which are the most preferred sites over Ir (1 1 1) according to our calculations (see Fig. 3) and previous experimental testing [36]. CH adsorption calculations by Abild-Pedersen et al. [37] reported that CH adsorbs preferentially on threefold sites (hcp or fcc). Previous work also indicated that CH over Pt (1 1 1) prefers hollow sites, with differences in energies between hpc and fcc sites less than 0.1 eV [26,38]. Fig. 2 shows CO and CH geometries. The adsorbed CHCO geometry had the CH group near a hcp site, so only CH in the hcp position was modeled. The initial geometry of adsorbed CHCO we used was based on the work of Alcala et al. [15]. This geometry

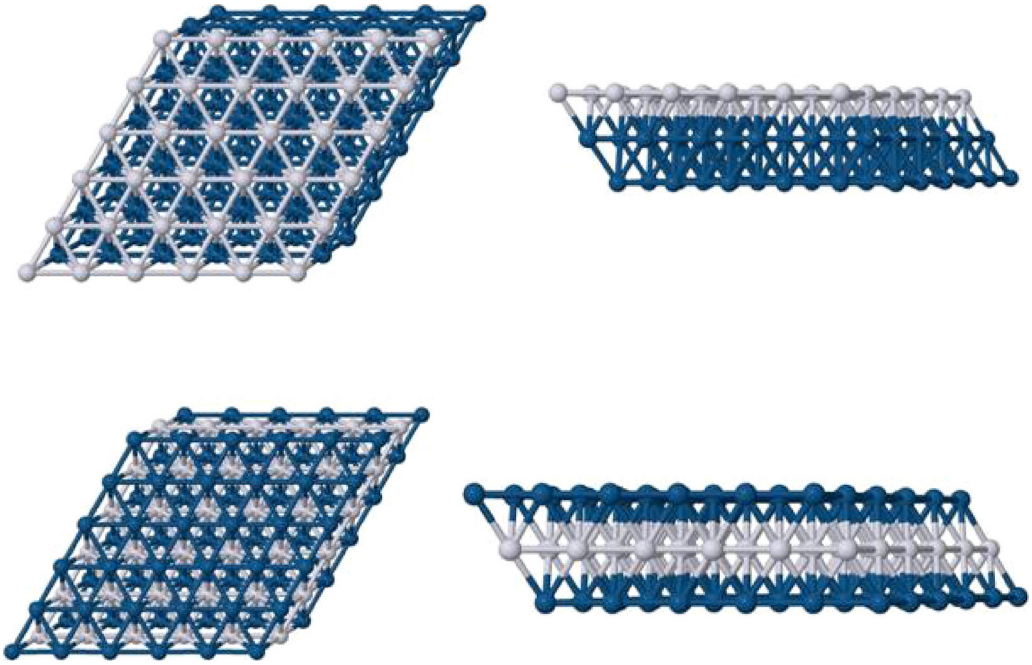

Fig. 1. Ir (1 1 1) alloyed surface showing a Pt/Ir overlayer structure (top) and Pt/Ir underlayer structure (bottom). Side and front views are shown. Pt and Ir atoms are, respectively, gray and blue.

however did not necessarily converge to a stable configuration on several alloys, so we modeled several other initial geometries for these alloys, which involved the two C atoms either in top, bridge, or hollow sites. The energies for the most stable configurations are presented in the current paper.

2.1.3. Model verification

CP2K has previously been used to model Pt [39], where calculated surface and bulk properties of platinum were found comparable to previous literature results. We also conducted our own tests in order to validate our approach. In Fig. 3, we compare our adsorption results over Ir to those obtained by Krekelberg et al. [36]. They used a four-layer Ir (1 1 1) slab, periodically repeated in a 2×2 unit cell with five equivalent layers of vacuum between the metal slabs. Similar to our work, adsorption was only allowed on one side of the slab and the first layer of metal atoms was fixed in the bulk positions. Krekelberg et al. used a plane wave basis set and the PW91 exchange correlation functional0]. Our results for adsorption energies do not differ by more than 10% from this previous work, confirming the adequacy of our simulation method.

2.1.4. Linear scaling correlations

Calculating activation energies from an initial and final state can be very computationally time-consuming, and therefore several attempts have been made to develop empirical correlations to determine activation barriers. The general idea of the linear scaling correlations (often referred to as Brønsted Evans Polanyi or BEP correlations) is to express the energy of the transition state (E_{TS}) as a function of the difference in energy between the final and initial state of a reaction, or reaction energy ΔE_{rxn}. The accuracy and utility of these correlations have been demonstrated by several authors [15,16,18,27,41]. For this work we took advantage of these linear-scaling to calculate activation energies for C—C bond breaking of CHCO. We used the parameters published by Wang et al. [27], which gives the following equation:

$$E_{TS} = \gamma E_{diss} + \xi, \quad (4)$$

with $\gamma = 0.85$ eV and $\xi = 2.05$ eV. E_{TS} is the transition state energy and E_{diss} is the dissociation energy (reaction energy) for CHCO. Both are referenced relative to the reactant molecule in the gas-phase, so E_{diss} is defined by the following formula:

$$E_{diss} = E_{CO\text{-}surface} + E_{CH\text{-}surface} - 2E_{surface} - E_{CHCO\text{-}gas}. \quad (5)$$

$E_{CO\text{-}surface}$ is the energy of the surface with adsorbed CO, $E_{CO\text{-}surface}$ is the energy of the surface with adsorbed CH, $E_{surface}$ is the energy of the bare surface, and $E_{CHCO\text{-}gas}$ is the energy of a gas-phase CHCO molecule.

2.2. Experimental methodology

2.2.1. Synthesis of Ir, $Ir_{80}Rh_{20}$, $Ir_{77}Ru_{23}$ nanoparticles

Carbon supported Ir, $Ir_{80}Rh_{20}$, and $Ir_{77}Ru_{23}$ nanoparticles were prepared via the Polyol method with or without the presence of surfactant Polyvinylpyrrolidone (PVP) as stablizing agent. In a typical synthesis of Ir nanoparticles, 28.2 mg of hydrous $IrCl_3$ (0.08 mmol, Alfa Aesar, 99.9%) was dissolved in 3 ml ethelyne glycol (EG, Mallinckrodt Chemicals) upon sonication, and then injected into a pre-heated (170 °C) 50 ml three-neck flask containing 8 ml of EG solution. The reaction proceeded for 30 min to allow the complete reduction of Ir^{3+} into Ir metal. Similarly, for the synthesis of Ir_4Rh_1 nanopariticles, a 4 ml EG mixture containing 28.2 mg of hydrous $IrCl_3$ (0.08 mmol) and 8.6 mg of K_3RhCl_6 (0.02 mmol, Alfa Aesar, 99.99%) was injected into the pre-heated (170 °C) 50 ml three-neck flask containing 7 ml of EG solution. In the synthesis of $Ir_{77}Ru_{23}$, 31.8 mg of hydrous $IrCl_3$ (0.09 mmol, Alfa Aesar, 99.9%) and 8.0 mg of hydrous $RuCl_3$ (0.03 mmol, Alfa Aesar, 99.9%) metal precursors were dissolved in 4 ml of EG and injected into 7 ml of hot EG (170 °C) which contained 55 mg of PVP. We allowed 30 min to complete the reaction. These resulting particles were then mixed with active carbon (Vulcan, XC-72R) at room temperature (RT) for 1 h, washed with copious ethanol and DI water, and dried out under vacuum at RT. The $Ir_{77}Ru_{23}$/C was further treated at 300 °C in air followed by H_2 flow at 100 °C using a tube furnace to remove residual surfactant [26].

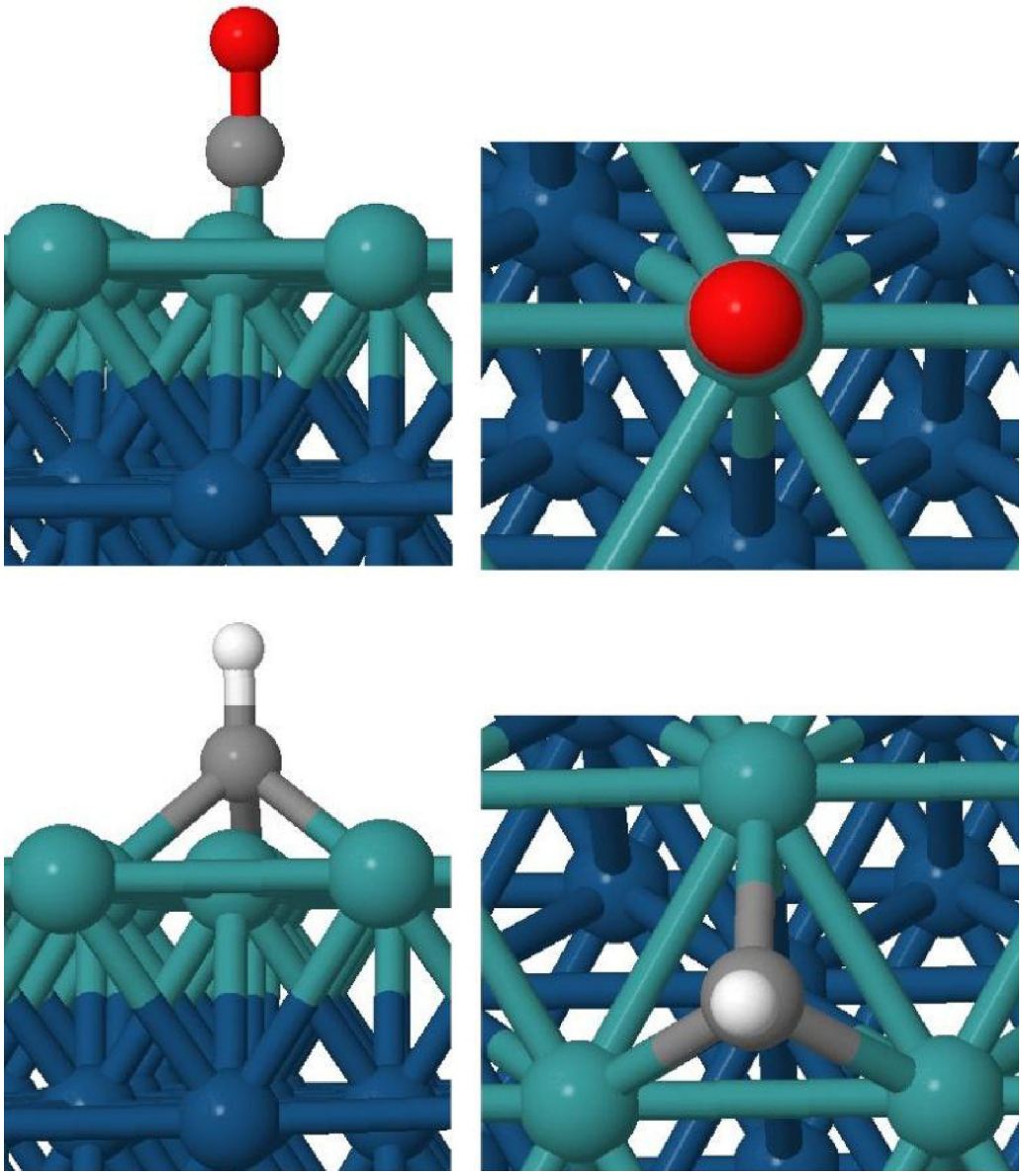

Fig. 2. Top and side views of CH and CO adsorption.

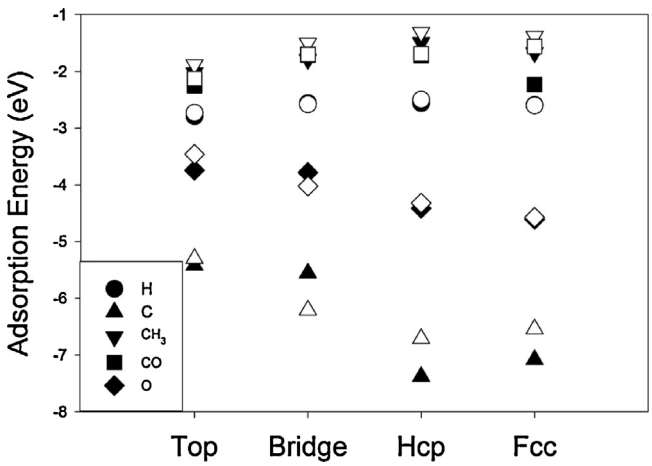

Fig. 3. Comparison of adsorption energies (in eV) for H, CH, CH_3, CO and O over Ir (1 1 1) surface slabs. Filled markers correspond to our work while the unfilled markers correspond to values extracted from Krekelberg et al. [36].

2.2.2. Electrochemical measurements

The electrochemical properties of carbon supported Ir, Ir_4Rh_1, $Ir_{77}Ru_{23}$ and commerical Pt/C (ETEK) catalysts were evaluated using a CHI 660 single channel electrochemical workstation (CH instruments, Inc.). The three-electrode system composed of a glassy carbon working electrode (rotating disc electrode, RDE), a platinum wire counter electrode and an Ag/AgCl (1 M KCl) reference electrode was employed for the test. All the Ir-based electrocatalysts were prepared in de-ionized water making a 2.5 mg/ml suspension while the commercial Pt/C (ETEK, 20 wt.% of Pt) water dispersion was made as 1.25 mg/ml by sonication. A volume of 10 μl catalyst ink was drop-casted on the RDE to form a thin layer of catalyst. Upon drying in a vacuum, another 10 μl of Nafion solution (0.5%, $V_{0.5\ wt\%\ Nafion}$:V_{water} = 0.05 ml:10 ml) was dropped on top of the catalyst layer and dried prior to the electrochemical tests. The rotating rate of the RDE was controlled at 1000 rpm. Blank cyclic voltammetry (CV) was firstly performed in a Ar-purged 0.5 M sulfuric acid (99.999%, Sigma-Aldrich) solution recording from −0.25 V to 0.35 V. The electrochemically active surface areas (ECASAs) of Ir-based catalysts were estimated by choosing −0.22 V vs. Ag/AgCl as the lower

boundary for integration of charge in the backward scan. We note that the $Ir_{77}Ru_{23}$ only showed poorly defined features around the H adsorption/desorption region and the lower boundary for integration of charge was somewhat arbitrary. The charges of 220 μC/cm^2 and 210 μC/cm^2 for a monolayer of H adsorption/desorption were used in ECSA calculations for Ir–Ru/C catalysts and Pt/C, respectively.

The polarization curves and chronoamperometry measurements (CA) of those electrocatalysts were also conducted in 0.5 M H_2SO_4/0.5 M ethanol solution. The first cycles in CV measurements were recorded from −0.1 V to 0.35 V to determine their catalytic activity toward ethanol oxidation. The potential sweeping rate was kept at 30 mV/s for all the CV measurements. The potential was held at 0.3 V for Ir/C, Ir_4Rh_1/C, and Pt/C for 1 h in the CA measurements right after the completion of polarization curves. The applied potential however, was held at 0.2 V for $Ir_{77}Ru_{23}$/C in the CA measurement. All the electrochemical measurements were performed at ambient room temperature and the potentials were reported with respect to Ag/AgCl (1 M KCl) unless otherwise specified. The CA and CV plots presented in this work are the averaged data after at least six repeats with high reproducibility. The electrolyte was de-aerated by bubbling Ar 30 min prior to the measurements.

3. Results and discussion

3.1. Segregation of the alloy

The first step of our approach was to examine which of the two structures (overlayer and underlayer, see Fig. 1) under consideration were the most stable. To evaluate the relative stability of the two structures, we calculated the segregation energy associated with each transition metal by the following:

$$E_{seg} = \frac{E_{overlayer} - E_{underlayer}}{n_{atom}}, \quad (6)$$

where $E_{underlayer}$ is the calculated energy of the underlayer alloy structure, $E_{overlayer}$ is the energy of the overlayer alloy structure, and n_{atom} is the number of atoms in the slab. The calculated segregation energies are given in Table 1. Positive segregation energy indicates that the underlayer structure is preferred while negative segregation energy indicates that the overlayer structure is preferred. The segregation energy is thus an indicator of the strength of interaction between the metal alloyed with iridium. For instance, gold and silver have very strong negative segregation energies, indicating that these elements would prefer to segregate and potentially separate from an iridium alloy. Many early transition metals have positive segregation energies, indicating that alloying with iridium is thermodynamically feasible.

Previous similar calculation results can be found in the literature, such as by Ruban et al. [35]. Our definition of the segregation energy is slightly different from theirs since they calculated the segregation energy based on an iridium structure with only one impurity atom in the top or second layer. Nevertheless their work presents a good comparison with our calculations. Their results are shown in parenthesis in Table 1 and typically are in good agreement with our results. The general trend for the segregation energy is that the values decrease as one moves toward the right of the periodic table, or that late transition metals have a greater preference to segregate from iridium.

3.2. Adsorption energies

3.2.1. CO

CO is a potential poison for fuel cell catalysis, so understanding how resistant potential catalysts are to CO is crucial to identifying viable Pt replacements. Any potential catalyst should not suffer from CO poisoning problems like Pt. We therefore utilized DFT calculations to establish whether CO poisoning is an issue worth considering for Ir-based alloys. CO is also a product of CHCO scission, so binding energies for CO can be used to calculate activation energies for the C—C bond breaking. According to our calculations and previous work [36], the most stable adsorption site for CO over a pure iridium (1 1 1) slab was the top site, as indicated by Fig. 3. We thus chose to model CO in the top site over our iridium-based surfaces, and our results are reported in Table 2. As a reference, we calculated the CO adsorption energy on a pure Pt (1 1 1) surface (using a similar cell to those shown in Fig. 1) to be −2.17 eV. As a first approximation, this value serves as a benchmark on whether a catalyst is more or less CO-resistant than Pt, based on whether the adsorption energy over the alloy is higher or lower than this value. We note that two values in the table are based on modified calculations, namely the values for the underlayer Ir–Co and Ir–Ni alloys. These calculations did not converge to a stable geometry after many iterations and attempts, indicating that such a system is relatively unstable, possibly due to the alloy configuration. We thus froze the alloy surface during optimization of CO adsorption similar to previous work [18] which showed minimal effect due to full relaxation. These values thus are not fully correct since surface relaxation is ignored, but do provide a first estimate of CO adsorption values. We also do not include results for the Ir–Zr overlayer structure since this alloy was severely distorted from the model (1 1 1) surface structure and thus not representative of a real alloy. Several adsorbed structures also did not converge (discussed further in the paper) indicating that the alloy model we used, a simplistic way to consider near surface alloys, likely requires further refinement. Such refinement of the alloy structures however is beyond the scope of the current work. Nonetheless, as our results will show, the trends in Ir-based alloy reactivity provide important insight into catalyst development. All the underlayer bimetallic structures involving early transition metals have CO adsorption energies smaller in magnitude than over Pt, while the underlayer structures for later transition metals have CO adsorption energies more negative than over Pt (with the exception of Au). For the underlayer structures, the CO binding energy tends to increase when moving to the right of the periodic table. The underlayer structures are more stable for metals of group 8 and lower (see Table 1) and these preferred alloys all have smaller CO binding energies than Pt, suggesting several alloys with stable structures that are more CO-resistant than Pt. As a point of comparison, recent experimental results by Du et al. [26] indicated that an Ir/Ru alloy demonstrated superior CO anti-poisoning ability compared to Pt. For the underlayer structures, the effect of alloying is largely electronic. The top surface layer is still Ir, but the sub-surface layer alters the electronic orbitals of the Ir atoms sufficiently to weaken or strengthen CO binding. The trends in the overlayer structures are not so apparent. Several group 4 (V, Cr, Mn) and group 6 (W, Re, Os, Ir) metals show increased CO adsorption relative to Pt, while all group 5 metals having the overlayer structure have CO adsorption energies less exothermic than Pt. There is no apparent trend when moving across the periodic table. The top layers of the alloys are composed of the substituted metal, so the presence of the sub-surface Ir modifies the electronic structure of the substituted metals, but the trends in this effect are not clear. We note that CO adsorption energies for the Au alloys are all very low. Au is known to generally be inert, except typically for nano-sized particles, which is consistent with these results. We also note that the CO adsorption energy over all the preferred alloy structures, that is the energetically most stable alloys (either overlayer or underlayer) according to Table 1, have CO adsorption energies lower in magnitude than pure Pt (with the exception of pure Ir, Ir/Cu and Ir/Pt), indicating that several Ir-M alloys may be more resistant to CO than pure Pt. Our DFT results show that CO poisoning is less of

Table 1
Calculated segregation energies as calculated according to Eq. (6). Energies are given in eV. Segregation energies calculated by Ruban et al. [35] are given in parenthesis. Dark shaded cells correspond to alloys where the underlayer structure is preferred, or the segregation energy is positive.

Ti	V	Cr	Mn	Fe	Co	Ni	Cu
0.53 (0.29)	0.55 (0.51)	0.50 (0.35)	0.36 (0.09)	0.20 (0.11)	0.16 (0.16)	0.07 (0.12)	−0.12 (−0.12)
Zr	Nb	Mo	Tc	Ru	Rh	Pd	Ag
0.36 (−0.43)	0.42 (0.10)	0.43 (0.35)	0.23 (0.35)	0.09 (0.23)	−0.04 (−0.08)	−0.22 (−0.55)	−0.30 (−1.00)
Hf	Ta	W	Re	Os	Ir	Pt	Au
0.42 (−0.17)	0.50 (0.26)	0.48 (0.47)	0.25 (0.48)	0.12 (0.32)	0.00 (0.00)	−0.21 (−0.58)	−0.43 (−1.20)

Table 2
CO adsorption energies on both under- and overlayer alloy surfaces. Shaded values correspond to alloys where CO binds more strongly than on pure platinum. Pure Pt has a calculated adsorption energy of −2.17 eV. All energies are given in eV. Adsorption energies for the Ir–Zr overlayer structure are not given due to the extreme distortions observed in the Ir–Zr surface.

	Ti	V	Cr	Mn	Fe	Co	Ni	Cu
Overlayer	−2.07	−2.48	−2.59	−2.73	−1.94	−1.97	−1.92	−1.10
Underlayer	−1.66	−1.71	−1.55	−1.70	−1.96	−1.06	−1.53	−2.43
	Zr	Nb	Mo	Tc	Ru	Rh	Pd	Ag
Overlayer	–	−1.92	−2.07	−2.01	−2.10	−1.96	−1.44	−0.39
Underlayer	−1.71	−1.60	−1.63	−1.99	−2.00	−2.27	−2.58	−2.61
	Hf	Ta	W	Re	Os	Ir	Pt	Au
Overlayer	−1.79	−2.08	−2.30	−2.21	−2.35	−2.25	−1.63	−0.63
Underlayer	−1.66	−1.66	−1.55	−1.97	−1.98	−2.25	−2.38	−0.13

a problem for most Ir-based alloys compared to Pt as indicated by lower CO adsorption energies for the majority of the studied alloys.

3.2.2. CH

Literature studies strongly suggest that CH preferably adsorbs at hollow sites [37,42]. Similar to our approach with CO adsorption in which top sites were considered, we modeled adsorption of CH over hcp sites for the alloys under consideration. Our calculated CH adsorption energies are reported in Table 3. Most adsorption energies appear to be near −6 to −7 eV. A few notable exceptions appear in the results. Binding energies for the Cr overlayer and Mn underlayer/overlayer structures appear to be unrealistically large (<−17 eV) and are thus not reported. These unrealistic values are likely indicative of the unstable nature of the alloy structure. We have modeled only underlayer and overlayer structures, which are simplistic representations of the alloy surface. More stable, complicated structures may exist for these alloys. In the case of the Ir–Zr overlayer alloy surface CH binding (also not reported) the alloy structure distorted significantly. Again, these distortions are likely indicative that the Ir–Zr alloy overlayer structure that we employed is simplistic and may not be representative of an actual Ir–Zr alloy surface. The models we used, the inclusion of an entire overlayer or underlayer of alloyed metals into an iridium slab, may have significant strain for some alloy combinations. These alloy models, however, allow a computationally fast approach to modeling and comparing many alloy combinations.

3.2.3. CHCO

The initial geometry that we used for CHCO was the geometry identified by Alcala et al. [15] over a Pt (1 1 1) surface. This initial geometry appeared to be stable when the surface was made of a platinum group metals, and thus all CHCO adsorption energies for the underlayer structures were calculated with CHCO in the configuration presented on Fig. 4a. In this geometry the CO is oriented in a top-like position, while the CH is oriented in a bridge-like position. For the overlayer structures, two different structures were identified as stable. The first geometry was the one proposed in Ref. [15] that is displayed in Fig. 4a, and was encountered with underlayer structures and overlayer structures involving platinum group metals the second geometry is represented in Fig. 4b for the case of a Ti overlayer and was more stable for all the other overlayers structure not involving platinum group metals. This geometry had the two C atoms in hollow-like positions. A summary of our results is found in Table 4.

Adsorption energies of CHCO varied between −1.7 and ∼−7 eV. Again a few problems were encountered in the simulations. CHCO adsorption over the silver and gold overlayer structures did not reach a stable structure where both C atoms were bound to the surface, despite modeling a number of different initial geometries. In these cases the CHCO adsorbate converged to a geometry where only the carbon atom linked to the hydrogen atom was bound to the surface, while the second carbon atom moved away from the surface. These surfaces are apparently resistant to CHCO

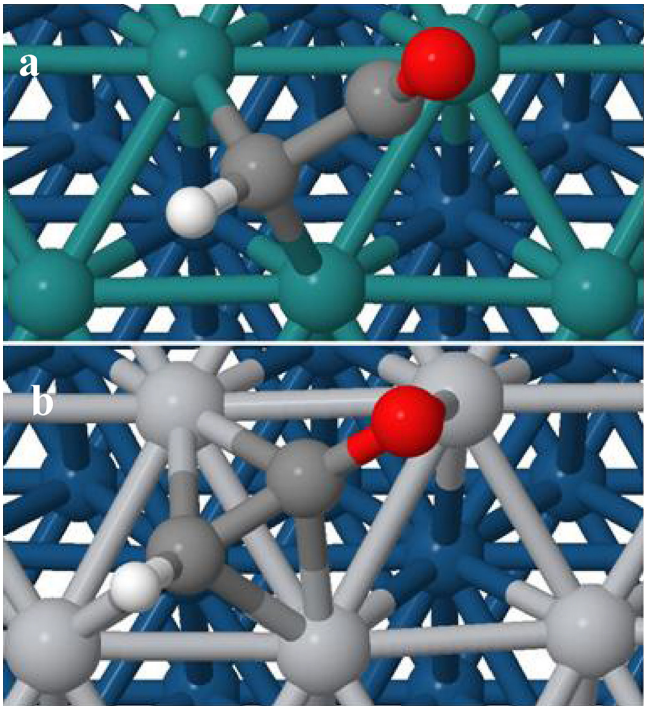

Fig. 4. (a) CHCO geometry on a Ru/Ir overlayer structure. (b) CHCO geometry on a Ti/Ir overlayer structure. Ruthenium, titanium, iridium, carbon, oxygen and hydrogen atoms are, respectively, turquoise, light gray, blue, dark gray, red and white. (For interpretation of the references to color in this figure legend, the reader is referred to the web version of this article.)

Table 3
CH adsorption energies on both under- and overlayer structures. Energies are given in eV. Adsorption energies for the Ir–Mn alloys, Ir–Cr overlayer, and Ir–Zr overlayer are not given due to difficulties in alloy stability as discussed in the text. Pure Pt has an adsorption energy of −7.46 eV. Shaded values correspond to alloys where CH binds more strongly than on pure platinum.

	Ti	V	Cr	Mn	Fe	Co	Ni	Cu
Overlayer	−7.36	−8.58	–	–	−6.71	−6.98	−6.68	−4.82
Underlayer	−6.51	−6.48	−7.92	–	−6.64	−7.91	−6.47	−8.72
	Zr	Nb	Mo	Tc	Ru	Rh	Pd	Ag
Overlayer	–	−6.71	−7.15	−6.91	−6.96	−6.71	−5.75	−3.20
Underlayer	−7.06	−6.81	−5.99	−6.57	−6.72	−6.91	−7.62	−8.09
	Hf	Ta	W	Re	Os	Ir	Pt	Au
Overlayer	−6.69	−7.13	−7.45	−7.25	−7.22	−6.94	−6.09	−3.99
Underlayer	−6.96	−6.83	−5.86	−6.61	−7.41	−6.94	−7.17	−8.48

adsorption (as indicated by the lowest adsorption energies of the overlayer structures), and are therefore expected to have low catalytic activity. The adsorption energies of CHCO over the Ir–Cr overlayer and Ir–Mn structures are all extremely exothermic to the point of being unrealistic (<−15 eV), which indicates that these alloy structures are likely unstable and/or unrealistic models, as already discussed in the section on CH adsorption (see above). We therefore do not consider these adsorption energies reliable and do not use these values in further analysis. Zr and Hf overlayer structures demonstrated large buckling at the surface leading to very unrealistic structures. The strongly deformed structures showed that the overlayer structures were an unlikely realistic model due to strain so we also did not consider results from these two geometries further in this paper. Generally, for a class of reactions the more stable an adsorbed intermediate is (as manifested through the adsorption or reaction energy), the lower the activation energy. This is mathematically constructed as a linear scaling relationship (see Eq. (4)). Our calculated adsorption energy of CHCO was found to be −4.15 eV over Pt (1 1 1). Several alloys have more exothermic adsorption energies compared to Pt. These are overlayer structures of early transition metals and a few underlayer structures of late transition metals. On some of these surfaces the CHCO adsorption energies are more exothermic by 1 or more eV compared to Pt. On the other hand for many alloys (most underlayer and late transition metal overlayer structures) CHCO is less stable than over Pt, with adsorption energies typically near −2 to −3 eV.

3.3. Effects of adsorbates on segregation

The reaction environment may change the thermodynamically preferred state of the alloy. For example Greeley and Mavrikakis [11] showed that hydrogen adsorption could induce segregation in select alloys. Other work also showed that the presence of adsorbates can alter segregation preferences [43–45]. Determining how the reaction environment affects segregation is crucial for designing and understanding stable catalysts. We thus calculated segregation energies in the presence of CO. The segregation energy of a bare surface represents the relative stability of the underlayer and overlayer structures in the absence of adsorption. When an adsorbate is present, the energy released upon adsorption may be such that the segregation trend changes. This is illustrated in Fig. 5 for an Ir/V alloy. The bare segregation energy is 0.55 eV, indicating that the underlayer structure is preferred. The adsorption energies for CO over the overlayer and underlayer structures are −1.71 and −2.48 eV, respectively. There is 0.77 eV more energy released when CO is adsorbed on the overlayer alloy, which is more than the segregation energy of 0.55 eV. Consequently, CO adsorption may induce the migration of the sub-layer V atoms toward the surface. The net effect is a gain of 0.22 eV (0.77–0.55 eV) when the segregation occurs.

In Fig. 6 we have plotted the bare segregation energies versus the difference in CO adsorption energies between overlayer and underlayer structures. This plot shows which alloys may undergo a change in segregation preference in the presence of CO, as indicated by the gray areas. The majority of bare alloys prefer to form underlayer structures (positive segregation energies). However over most of the alloys CO prefers to bind to overlayer structures. There are a number of alloys where this preference may induce segregation upon CO adsorption, such as Os, W, or V. Other alloys (involving Ru, Re, and Mo) have segregation energies close to the CO adsorption energy differences, so it is difficult to determine whether segregation may actually occur. A few bare alloys (Pt and Rh) prefer the overlayer structure, but upon CO adsorption prefer the underlayer structure. Our results have only considered select alloy structures and one adsorbate, but do show that segregation trends for Ir–M alloys can change due to environmental conditions. Such effects may be useful for catalyst synthesis and also may affect catalyst stability.

3.4. Alloying and surface chemistry

There are two major effects related to alloys that influence adsorption energies and surface chemistry [46,47]. The first is the strain effect. Because the bond lengths and lattice parameters are different for each metal, alloying may put strain on metal atoms as they adapt new bond lengths to fit into the parent metal. This strain induces changes in the electronic orbitals of the metals. For example, under tensile strain an upshift in the d-band occurs, while under compressive strain the d-band moves down in energy. These

Table 4
CHCO adsorption energies on both the under- and overlayer alloy structures. Energies are given in eV. Pure Pt has an adsorption energy of −4.15 eV. Shaded values correspond to alloys where CHCO binds more strongly than on pure platinum. Several values are not listed due to problems of convergence/distortion as discussed in the text.

	Ti	V	Cr	Mn	Fe	Co	Ni	Cu
Overlayer	−5.85	−7.09	–	–	−3.35	−4.34	−3.90	−2.42
Underlayer	−2.74	−2.56	−4.33	–	−3.09	−3.60	−2.74	−5.22
	Zr	Nb	Mo	Tc	Ru	Rh	Pd	Ag
Overlayer	–	−4.64	−4.76	−4.22	−3.21	−3.20	−2.90	−1.73
Underlayer	−3.00	−2.58	−2.30	−2.96	−3.03	−3.64	−4.26	−4.68
	Hf	Ta	W	Re	Os	Ir	Pt	Au
Overlayer	–	−5.22	−5.09	−4.26	−3.59	−3.58	−3.15	−2.24
Underlayer	−2.85	−2.58	−2.17	−3.07	−3.17	−3.58	−3.93	−5.33

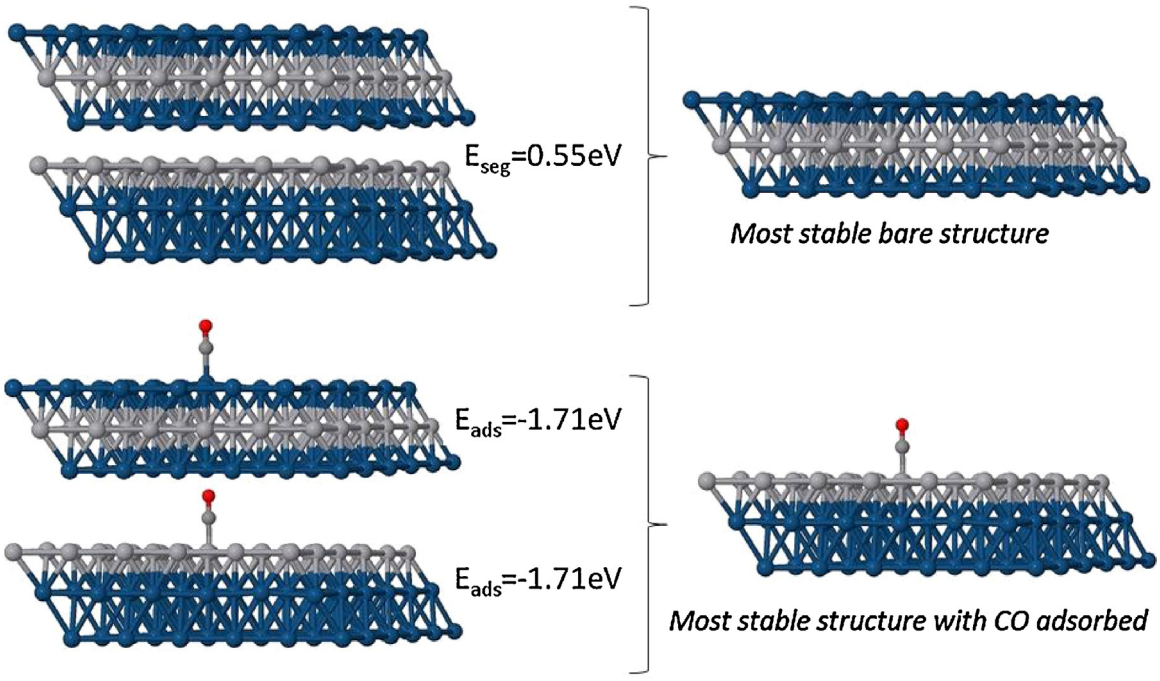

Fig. 5. Illustration of adsorbate-induced segregation for the case of an Ir/V alloy. The energy of adsorption over the overlayer structure is more negative than the adsorption energy over the underlayer structure by 0.77 eV, which is larger in magnitude than the segregation energy, and so the segregation trend is reversed.

shifts in d-band energies can weaken (downward d-band energy) or strengthen (upward d-band energy) adsorption. Such effects have shown and discussed in the literature (see for example the following references: [46,47–50]).

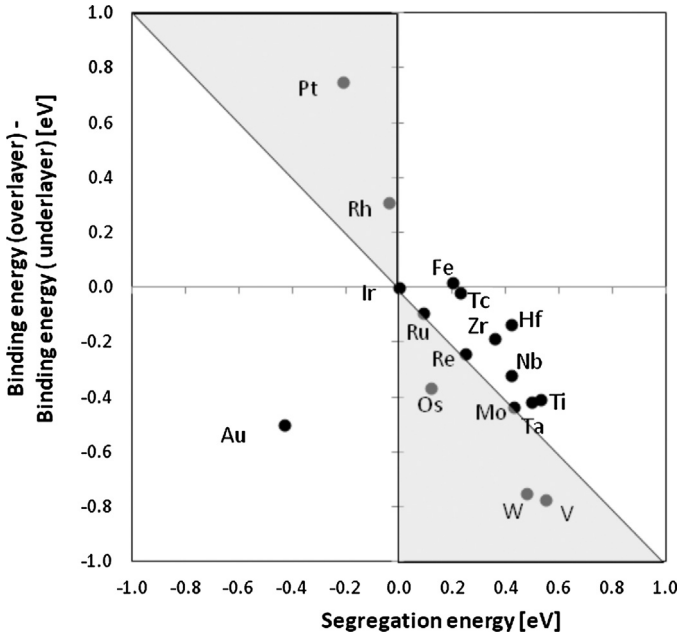

Fig. 6. Stability of bimetallic structures with respect to CO-induced segregation. The segregation energies indicate the most stable structures for the bare surfaces. Positive values correspond to alloys where the underlayer surface is preferred. Positive values for the difference in binding energy indicates that CO prefers to adsorb over the underlayer structure, while negative values indicate that CO prefers to adsorb over the overlayer structure. Alloys situated in the gray area are likely to undergo adsorbate-induced segregation. Alloys containing Pd, Ag, Cu and Mn are not represented on this figure for clarity purposes since they have a very high absolute value of their segregation energy and are situated either far right (Pd, Ag, Cu) or far left (Mn) on the graph in an area not influenced by adsorbate-induced segregation.

The second effect arises due to intrinsic electronic differences between two metals and is called the ligand effect. The presence of another nearby metal may alter the electronic structure of the metals due to new interactions between the metals. In the case of the underlayer structure, the top layer of Ir atoms are only under strain in the vertical direction (the surface lattice parameter is not changed) so the predominant change in adsorption is attributed to the ligand, or electronic, effect. In contrast, for the overlayer structure, the top layer of surface metal atoms may experience both strain and ligand effects. Thus, comparing the two alloy surface types may provide clues as to the role these two effects may have on catalysis.

We have plotted the adsorption energies for CO and CH over the underlayer (Figs. 7 and 8) and overlayer (Figs. 9 and 10) structures; the same data is presented in Tables 2 and 3. Our results show that for the underlayer structures stronger adsorption occurs for alloyed metals to the right of the periodic. These results can be explained in terms of the d-band model by Hammer and Nørskov [46]. Upon adsorption, bonding and anti-bonding states form between the

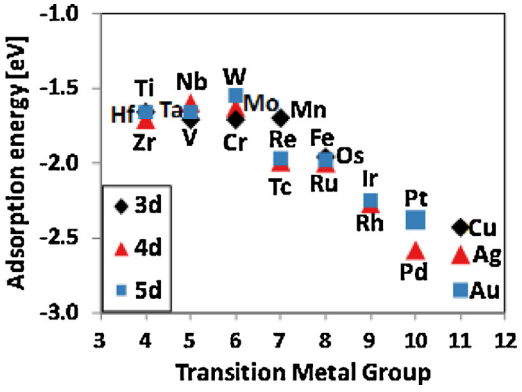

Fig. 7. CO adsorption energies over the underlayer (Ir/M/Ir) alloys. Adsorption energies are plotted relative to the respective position of the alloyed metal in the periodic table.

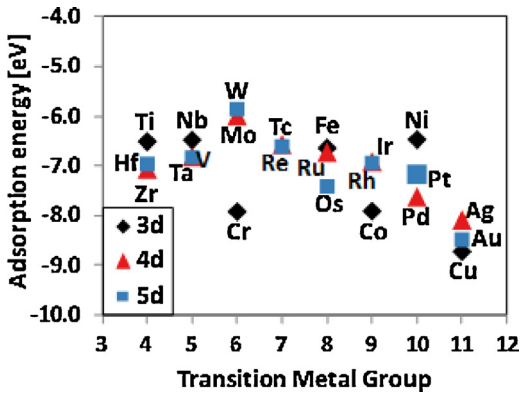

Fig. 8. CH Adsorption energies over the underlayer (Ir/M/Ir) alloys. Adsorption energies are plotted relative to the respective position of the alloyed metal in the periodic table. The Ir–Mn alloy is not included, as discussed in the text due to stability problems with CH adsorption.

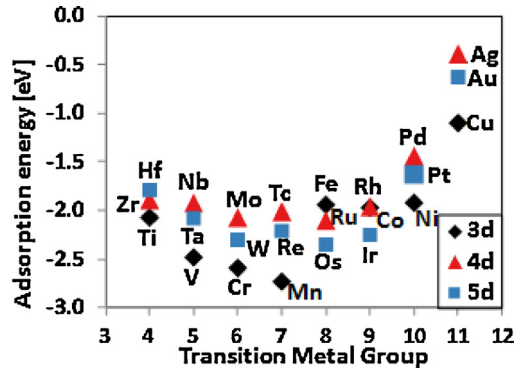

Fig. 9. CO adsorption energies over the overlayer (M/Ir/Ir) alloys. Adsorption energies are plotted relative to the respective position of the alloyed metal in the periodic table.

metal surface d electrons and adsorbate electrons. Higher d-band energies lead to more anti-bonding orbitals being above the Fermi level, and thus more anti-bonding states being unfilled. To compensate for the unfilled anti-bonding states, more filling of bonding states occurs. Thus, more stable adsorption occurs for surfaces with higher d-band energies. Kitchin et al. [47] modeled Pt surfaces where the second layer was replaced by another metal, analogous to our underlayer structures. They did indeed observe that alloying with late transition metals increased the d-band energy and thus would expected to decrease (stabilize) adsorption energies, which is similar to what we observe with Ir-based underlayer alloys. In

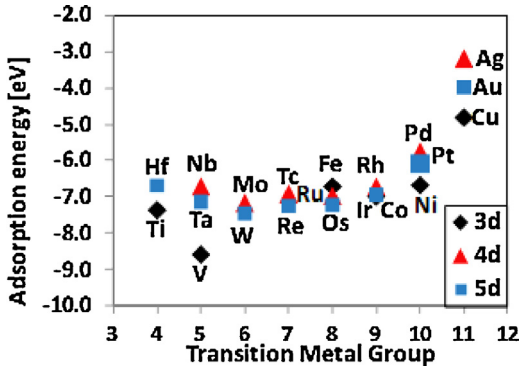

Fig. 10. CH adsorption energies over the overlayer (M/Ir/Ir) alloys. Adsorption energies are plotted relative to the respective position of the alloyed metal in the periodic table.

summary, our results indicate that the electronic or ligand effect induces changes in overlayer structures that favor adsorption over alloys with late transition metals.

With the overlayer structures, the adsorption energies obtained using the different transition metals are mainly constant, with the exception of the metals from group 11 (Au, Ag, Cu). These later elements typically bind CO weakly. Su et al. [8] investigated CO and O adsorption energies over surfaces having various platinum-based overlayer structures (albeit with less surface substitution) and found similar results in that the range of adsorption energies obtained was small (having a span of approximately only 0.1 eV for Cr, Mn, Fe,Co, Ni, and Cu overlayer structures). In contrast to results from the underlayer structures, late transition metal alloys in the overlayer configuration demonstrated the least stable adsorption energies, again reflecting the weak reactivity/adsorption of the later transition metals, i.e. noble metals, which are exposed on the surface. In the case of the overlayer structures the alloys behave more like the dopant metal rather than the parent metal (iridium). The exposed surface atoms experience both strain and ligand effects but such affects give no discernable trend on the adsorption energies. This is in contrast to the underlayer structures, where electronic effects have a clear effect on adsorption energies.

3.5. Activation energy of the ethanol oxidation reaction: C—C bond breaking

We used the transition state scaling relationship of Wang et al. [27] to calculate the activation energies for CHCO dissociation to CH and CO over the various alloys, as displayed in Table 5. We calculated the activation energy over Pt (1 1 1) to be 1.89 eV. As a point of comparison, our results compare favorably with previous work [26] that utilized a similar method, but with a four-layer slab. This previous work calculated activation energies over Pt, Ir–Ru, and Ir surfaces to be 1.69, 1.05, and 1.31 eV, respectively. In the current work we calculated activation energies to be 1.88, 1.42, and 1.69 eV for the three surfaces. The trends between the three surfaces are similar for both the current and previous work, but the exact energy differences can likely be attributed to the slab model choice (three versus four layers).

Almost all underlayer structures have lower activation energies than pure Pt, while only a few overlayer structures have activation energies less than Pt. Typical activation energies are lowered by 0.1–0.3 eV, but may be lowered as much as 0.8 eV (Ir–Os). These results suggest that sub-layer modification of Ir may lead to more facile C—C bond breaking, which is desirable for ethanol oxidation. The issue is further complicated because the alloy structure may change depending on the environment, as Section 3.3 shows. For several alloys segregation occurs in the presence of CO which may not occur in an otherwise vacuum environment. The actual environment will be much more complex with a large number of adsorbates so it is difficult to predict which alloy structure is thermodynamically preferred. Nonetheless, we have identified several candidate alloys that may oxidize ethanol with more efficiency than Pt. For example, Ir–Ru, Ir–Rh, and Ir–Os all have lower activation energies for C—C scission than Pt, regardless of the alloy structure. Our results reinforce the possibility of using iridium-based alloys as a primary component in EOR catalysts.

3.6. Toward an economically viable catalyst

In this work we have determined the adsorption energies of the different reaction intermediates and the activation energies for a potential rate-determining step of the EOR over various Ir–M catalysts. These values, or descriptors, allow the prediction of catalyst candidates for the EOR. The notion of descriptors in combination

Table 5
Activation energies for the reaction step CH + CO → CHCO over different Ir/M bimetallic structures using the BEP correlation from Wang et al. [27]. Pure Pt has an activation energy of 1.89 eV. Gray values correspond to higher activation energies than on a pure Pt. Energies are given in eV. Select values for Ir–Mn, Ir–Cr, Ir–Zr and Ir–Hf are not shown because of alloy stability problems, as discussed previously in the text.

	Ti	V	Cr	Mn	Fe	Co	Ni	Cu
Overlayer	3.76	3.66	–	–	1.89	2.64	2.49	3.20
Underlayer	1.68	1.48	2.20	–	1.68	1.88	1.83	1.73
	Zr	Nb	Mo	Tc	Ru	Rh	Pd	Ag
Overlayer	–	3.20	2.83	2.54	1.42	1.73	2.65	4.44
Underlayer	1.46	1.32	1.69	1.58	1.51	1.76	1.53	1.54
	Hf	Ta	W	Re	Os	Ir	Pt	Au
Overlayer	–	3.31	2.74	2.14	1.39	1.69	2.45	4.09
Underlayer	1.43	1.25	1.73	1.67	1.10	1.69	1.75	1.68

with modeling results is described by Nørskov et al. [51] where the value of DFT for screening catalysts is shown. A desirable ethanol oxidation fuel cell catalyst should be resistant to CO poisoning (e.g. low CO adsorption energy) and readily break apart ethanol (e.g. low activation energy for C—C breaking). A third descriptor could be the cost of the catalyst. The catalyst is a significant portion of the fuel cell's cost and cheaper catalysts may drive down the cost of the fuel cell significantly.

In Fig. 11, these three descriptors are gathered into one graph with the activation energy plotted against the CO adsorption. These values are taken from the most preferred structure (overlayer or underlayer determined by the segregation energy). The prices of the alloyed transition metals [52] are represented by the size of the spheres in the plot. We note that the two surface chemistry parameters (CO adsorption energy and activation energy) are not strictly independent. A catalyst with low CO adsorption energy will likely have large activation energy, since one of the final products (CO) is weakly bound to the surface and the reaction energy will therefore be more endothermic. A more endothermic reaction energy leads to higher activation energies in the BEP formalism (Eq. (4)). Similarly, more stable CO binding lowers the activation energy for CHCO dissociation. Because of this relationship, the data appears mostly linear with positive slope.

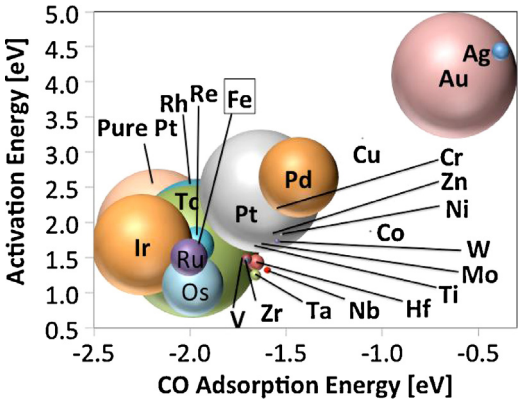

Fig. 11. Activation energies versus CO adsorption energy for the various studied alloys in their preferred configuration (underlayer or overlayer configuration as determined by most stable structure). The sphere sizes are proportional to metal prices [52].

Our calculations found that pure Pt has a CO adsorption energy of −2.17 eV and activation energy of 1.89 eV (indicated by the sphere to the left), and any catalysts to the right and below this sphere are of interest. There are a number of potential catalysts

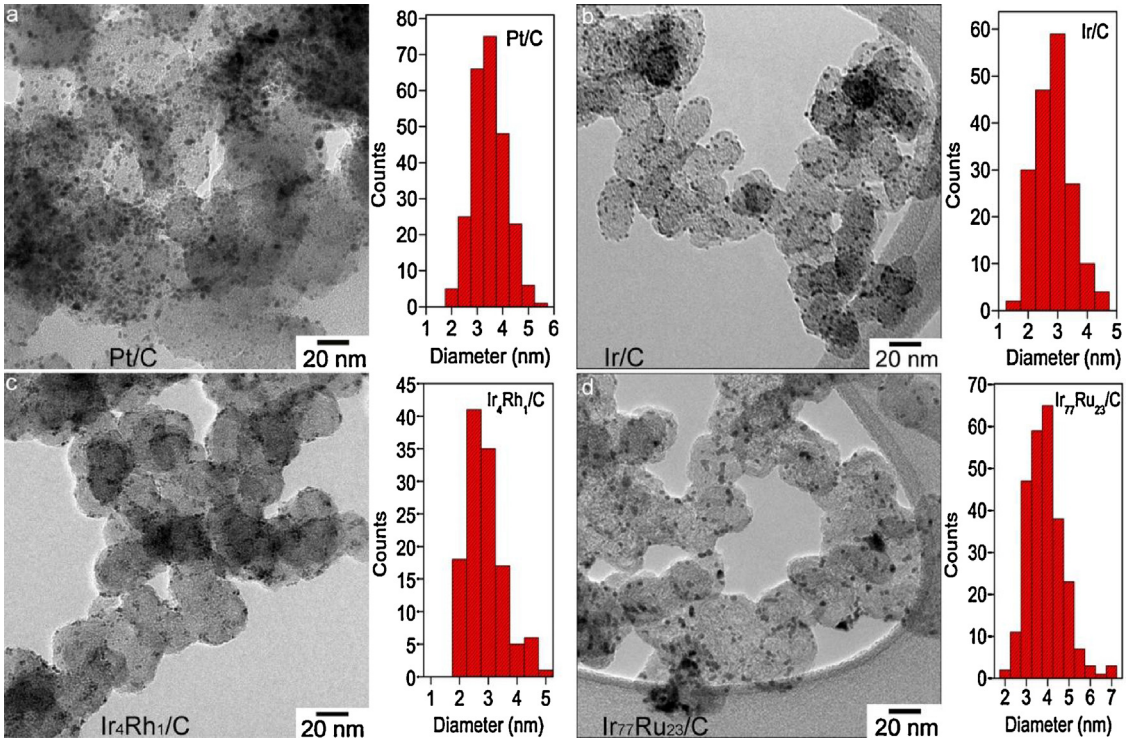

Fig. 12. TEM images of carbon-supported (a) Pt (ETEK), (b) Ir, (c) $Ir_{80}Rh_{20}$ and (d) $Ir_{77}Ru_{23}$ NPs along with their size distribution analysis. The Ir and $Ir_{80}Rh_{20}$ nanoparticles were prepared using surfactant-free method whereas $Ir_{77}Ru_{23}$ nanoparticles were made in the presence of surfactant PVP. See Section 2.2 for details.

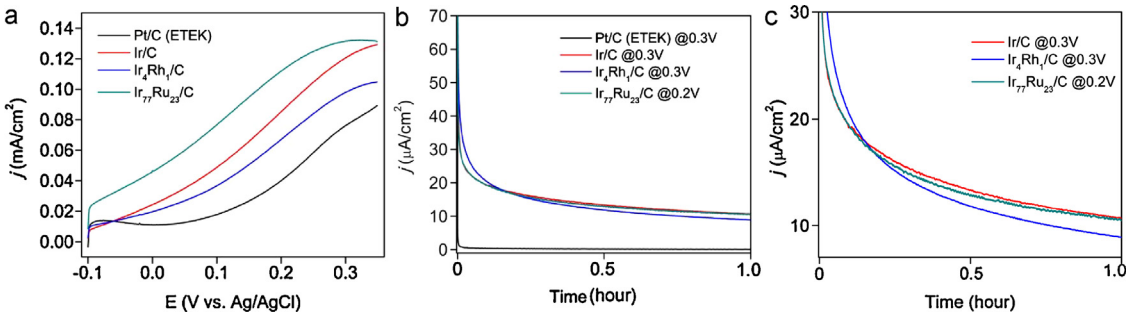

Fig. 13. (a) CV measurements (forward scan shown) of Pt/C (ETEK), Ir/C, Ir_4Rh_1/C along with $Ir_{77}Ru_{23}$/C sweeping from −0.1 V to 0.35 V vs. Ag/AgCl (1 M KCl) at a scan rate of 30 mV/s in 0.5 M H_2SO_4 + 0.5 M ethanol electrolyte. (b) Chronoamperometric (CA) measurements of above electrocatalysts at applied constant potential of 0.3 V or 0.2 V for a 1 h reaction in the same electrolyte at room temperature. (c) Zoom-in image of CA measurements shown in (b).

with CO adsorption energies between −2 and −1.5 eV that appear promising: Ir–Ru, Ir–Re, Ir–Os, Ir–Hf, Ir–Ta, Ir–Nb, etc. Further experimental work is needed to synthesize and test these catalysts. We must also admit that some of the identified catalysts may not even be stable under reaction conditions; segregation and/or oxidation are real possibilities for some of the alloys and further work is needed to assess this possibility.

3.7. Experimental analysis

The computational results indicate a number of viable catalysts for ethanol oxidation, which we have tested experimentally, namely Ir, Ir–Ru, Ir–Rh, and Pt (for comparison), all over carbon supports. Characterization of the synthesized particles by TEM, as given in Fig. 12, shows that all the Ir-based nanoparticles and commercial Pt nanoparticles were evenly distributed throughout the carbon support. The average sizes of Pt, Ir, Ir_4Rh_1 and $Ir_{77}Ru_{23}$ after analyzing at least 120 particles were calculated to be 3.2 ± 0.6, 2.6 ± 0.6, 2.6 ± 0.6, and 3.7 ± 0.8 nm, respectively. After heat treatment at 300 °C under open-air environment, all the carbon-supported catalysts remained in the form of nano-sized particles without agglomeration.

The catalytic activities of these Ir-based particles for the ethanol oxidation reaction were evaluated using CV and CA. Fig. 13a shows the CVs (forward scan) of the electrocatalysts in 0.5 M H_2SO_4/0.5 M ethanol electrolyte from −0.1 to 0.35 V vs. Ag/AgCl. All the Ir-based catalysts presented much enhanced ECSA-averaged current densities throughout the scanned potential range compared to the Pt/C electrocatalyst. In particular, the best performance by $Ir_{77}Ru_{23}$ showed ECASA-specific current densities of 0.112 and 0.131 mA/cm^2 at 0.2 V and 0.3 V vs. Ag/AgCl in CV, respectively, which are 180% and 70% higher than those of commercial Pt/C.

To evaluate the long-term catalytic activity of the Ir-based catalysts for the EOR, CA measurements were conducted in the same 0.5 M H_2SO_4/0.5 M ethanol electrolyte at a constant potential of 0.3 V or 0.2 V for 1 h (Fig. 13b). The current density initially dropped fast but gradually reached a quasi-steady state value. This could be due to the poisoning of active sites on the catalyst surface. After 1 h of reaction, all the Ir-based electrocatalysts exhibited superior long term activity compared to Pt/C. The $Ir_{77}Ru_{23}$ and Ir showed an ECASA—specific current density of ~10.5 μA/cm^2, which is about 10 times higher than that of Pt/C. The superiority of $Ir_{77}Ru_{23}$ for the EOR was even under-estimated as the CA was conducted at a potential of 0.1 V lower than that of Pt/C. Although the electroactivities of Ir, Ir–Ru and Ir–Rh nanocatalysts showed dramatic enhancement in EOR compared to commercial Pt catalysts, their performance is still inferior to state-of-art Pt-based binary and ternary catalysts, especially PtRh–SnO_2 [53,54] and PtIrSn [55] reported recently. Future work will evaluate other Ir-based electrocatalysts, especially the activity of Ir-based catalysts for splitting C—C bonds of ethanol. Our results herein are encouraging in that experimental results confirm the superiority of a select group of Ir-based catalysts.

4. Conclusions

Iridium-based bimetallic structures were investigated as potential candidates for replacing platinum as anode catalysts for the ethanol oxidation reaction. Overlayer (alloyed metal directly on surface) and underlayer (alloyed metal in subsurface position) structures made of a transition metal associated with iridium were used as idealized models of alloy surfaces. Density functional theory calculations were used to estimate two important descriptors: CO tolerance (e.g. CO adsorption energy) and activation energy for C—C scission. Breaking of strong C—C bonds is necessary for complete oxidation of ethanol. Based on previous work, we modeled dissociation of CHCO, a strong candidate for the rate-determining step. Underlayer structures demonstrated an enhanced CO tolerance in most cases with early transition metals being the most promising alloys. CHCO bond breaking also appeared to be more favorable on underlayer surfaces than on overlayer surfaces, always having a lower CHCO activation energy on an underlayer structure than on the overlayer structure for a given transition metal (with the exception of Ru and Rh where comparable energies were obtained). Moreover, underlayer structures generally exhibited better activation energy for CHCO dissociation than a pure platinum catalyst.

Combined with their good CO tolerance, iridium-based underlayer structure catalysts show excellent promise for the ethanol oxidation reaction. We identified several alloys (Ru–Ir, Rh–Ir, Nb–Ir, Hf–Ir, Ta–Ir, Zr–Ir, V–Ir) as promising catalysts. Overlayer structures also demonstrated good CO tolerance but their potential as an EOR catalyst was reduced by the relatively high activation energy for CHCO dissociation these alloys demonstrated. Our efforts have focused on screening potential catalysts, and further work is needed to determine whether such catalysts are stable under experimental conditions, evaluate full electrochemical environmental effects and determine full reaction pathways. Another limitation of our approach is that an ideal alloy model was used, and indeed several catalysts that we studied (i.e. Ir–Mn and Ir–Cr) demonstrated severe surface distortions upon adsorption, indicating that other, more stable structures are possible for these alloys. We have nonetheless identified several potential alloys that warrant more attention for direct ethanol fuel cells and our experimental work does indeed confirm that Ir alloys (e.g. Ir–Rh and Ir–Ru) may be superior ethanol oxidation catalysts to Pt.

Acknowledgment

We wish to thank the National Science Foundation (Grant no. CBET-1159662) (Award number 1159662) for financial support in this work.

References

[1] F. Vigier, S. Rousseau, C. Coutanceau, J.-M. Leger, C. Lamy, Top. Catal. 40 (2006) 111–121.
[2] S.a. Kirillov, P.E.S Tsiakaras, I.V. Romanova, J. Mol. Struct. 651–653 (2003) 365–370.
[3] F. Vigier, C. Coutanceau, A. Perrard, E.M. Belgsir, C. Lamy, J. Appl. Electrochem. 34 (2004) 439–446.
[4] W. Du, Q. Wang, D. Saxner, N.A. Deskins, D. Su, J.E. Krzanowski, A.I. Frenkel, X. Teng, J. Am. Chem. Soc. 133 (2011) 15172–15183.
[5] E. Antolini, J. Power Sources 170 (2007) 1–12.
[6] W. Du, K.E. Mackenzie, D.F. Milano, N.A. Deskins, D. Su, X. Teng, ACS Catal. 2 (2012) 287–297.
[7] F. Cell, J. Mann, N. Yao, A.B. Bocarsly, Langmuir 22 (2006) 10432–10436.
[8] H.-Y. Su, X. Gu, X. Ma, Y.-H. Zhao, X. Bao, W.-X. Li, Catal. Today 165 (2011) 89–95.
[9] J.-M. Léger, S. Rousseau, C. Coutanceau, F. Hahn, C. Lamy, Electrochim. Acta 50 (2005) 5118–5125.
[10] W. Zhou, Z. Zhou, S. Song, W. Li, Appl. Catal., B: Environ. 46 (2003) 273–285.
[11] J. Greeley, M. Mavrikakis, Nat. Mater. 3 (2004) 810–815.
[12] S. Alayoglu, A.U. Nilekar, M. Mavrikakis, B. Eichhorn, Nat. Mater. 7 (2008) 333–338.
[13] A.U. Nilekar, S. Alayoglu, B. Eichhorn, M. Mavrikakis, J. Am. Chem. Soc. 132 (2010) 7418–7428.
[14] M. Li, W. Guo, R. Jiang, L. Zhao, H. Shan, Langmuir 26 (2010) 1879–1888.
[15] R. Alcala, M. Mavrikakis, J.a. Dumesic, J. Catal. 218 (2003) 178–190.
[16] R. Alcala, J.W. Shabaker, G.W. Huber, M.A. Sanchez-castillo, J.A. Dumesic, P. Catalysts, J. Phys. Chem. B 109 (2005) 2074–2085.
[17] H. Xin, A. Holewinski, N. Schweitzer, E. Nikolla, S. Linic, Top. Catal. 55 (2012) 376–390.
[18] P. Ferrin, D. Simonetti, S. Kandoi, E. Kunkes, J.a. Dumesic, J.K. Nørskov, M. Mavrikakis, J. Am. Chem. Soc. 131 (2009) 5809–5815.
[19] L. Colmenares, H. Wang, Z. Jusys, L. Jiang, S. Yan, G.Q. Sun, R.J. Behm, Electrochim. Acta 52 (2006) 221–233.
[20] L. Jiang, G. Sun, S. Sun, J. Liu, S. Tang, H. Li, B. Zhou, Q. Xin, Electrochim. Acta 50 (2005) 5384–5389.
[21] C. Lamy, S. Rousseau, E.M. Belgsir, C. Coutanceau, J. Léger, Electrochim. Acta 49 (2004) 3901–3908.
[22] E. Christoffersen, P. Liu, A. Ruban, H.L. Skriver, J.K. NoØrskov, J. Catal. 199 (2001) 123–131.
[23] G. Camara, R. de Lima, T. Iwasita, Electrochem. Commun. 6 (2004) 812–815.
[24] V.M. Schmidt, R. Ianniello, E. Pastor, S. González, J. Phys. Chem. 100 (1996) 17901–17908.
[25] B.L. Cao, G. Sun, H. Li, Q. Xin, Fuel Cells Bull. 2007 (2007) 12–16.
[26] W. Du, N.a. Deskins, D. Su, X. Teng, ACS Catal. 2 (2012) 1226–1231.
[27] S. Wang, B. Temel, J. Shen, G. Jones, L.C. Grabow, F. Studt, T. Bligaard, F. Abild-Pedersen, C.H. Christensen, J.K. Nørskov, F.A. Claus, H.C. Jens, Catal. Lett. 141 (2010) 370–373.
[28] J. VandeVondele, M. Krack, F. Mohamed, M. Parrinello, T. Chassaing, J. Hutter, Comput. Phys. Commun. 167 (2005) 103–128.
[29] CP2K Open Source Molecular Dynamics, http://www.cp2k.org, Accessed 7/10/2014 (2014).
[30] J.P. Perdew, K. Burke, M. Ernzerhof, Phys. Rev. Lett. 77 (1996) 3865–3868.
[31] G. Lippert, J. Hutter, M. Parrinello, Mol. Phys. 92 (1997) 477–487.
[32] J. Vandevondele, J. Hutter, J. Chem. Phys. 127 (2007) 114105.
[33] S. Goedecker, M. Teter, J. Hutter, Phys. Rev. B: Condens. Matter 54 (1996) 1703.
[34] M. Krack, Theor. Chem. Acc. 114 (2005) 145–152.
[35] A. Ruban, H. Skriver, J. Nørskov, Phys. Rev. B: Condens. Matter 59 (1999) 15990–16000.
[36] W.P. Krekelberg, J. Greeley, M. Mavrikakis, J. Phys. Chem. B 108 (2004) 987–994.
[37] F. Abild-Pedersen, J. Greeley, F. Studt, J. Rossmeisl, T. Munter, P. Moses, E. Skúlason, T. Bligaard, J. Nørskov, Phys. Rev. Lett. 99 (2007) 4–7.
[38] D.C. Ford, Y. Xu, M. Mavrikakis, Surf. Sci. 587 (2005) 159–174.
[39] G. Santarossa, A. Vargas, M. Iannuzzi, C.A. Pignedoli, D. Passerone, A. Baiker, J. Chem. Phys. 129 (2008) 234703.
[41] J.E. Sutton, D.G. Vlachos, ACS Catal. 2 (2012) 1624–1634.
[42] I.M. Ciobıca, F. Frechard, R.A. van Santen, A.W. Kleyn, J. Hafner, Chem. Phys. Lett. 311 (1999) 185–192.
[43] G.E. Ramirez-Caballero, P.B. Balbuena, Chem. Phys. Lett. 456 (2008) 64–67.
[44] M. Kettner, W.B. Schneider, A.a. Auer, J. Phys. Chem. C 116 (2012) 15432–15438.
[45] G.E. Ramı, Y. Ma, R. Callejas-Tovar, P.B. Balbuena, G.E. Ramírez-Caballero, Phys. Chem. Chem. Phys. 12 (2010) 2209–2218.
[46] B. Hammer, J.K. Nørskov, Adv. Catal. 45 (2000) 71–129.
[47] J.R. Kitchin, J.K. Nørskov, M.a. Barteau, J.G. Chen, J. Chem. Phys. 120 (2004) 10240–10246.
[48] A. Ruban, B. Hammer, P. Stoltze, H.L. Skriver, J.K. NoØrskov, J. Mol. Catal. A: Chem. 115 (1997) 421–429.
[49] M. Mavrikakis, B. Hammer, J.K. Nørskov, Phys. Rev. Lett. 81 (1998) 2819–2822.
[50] J.G. Chen, C.A. Menning, M.B. Zellner, Surf. Sci. Rep. 63 (2008) 201–254.
[51] J.K. Nørskov, T. Bligaard, J. Rossmeisl, C.H. Christensen, A.M. Design, Nat. Chem. 1 (2009) 37–46.
[52] MetalPrices.com, http://www.metalprices.com, Accessed 11/20/2012 (2012).
[53] A. Kowal, M. Li, M. Shao, K. Sasaki, M.B. Vukmirovic, J. Zhang, N.S. Marinkovic, P. Liu, A.I. Frenkel, R.R. Adzic, Nat. Mater. 8 (2009) 325–330.
[54] W. Du, Q. Wang, C.a. LaScala, L. Zhang, D. Su, A.I. Frenkel, V.K. Mathur, X. Teng, J. Mater. Chem. 21 (2011) 8887.
[55] M. Li, D.a. Cullen, K. Sasaki, N.S. Marinkovic, K. More, R.R. Adzic, J. Am. Chem. Soc. 135 (2013) 132–141.